Converting Brownmillerite to Alternate Layers of Oxygen Deficient and Conductive Nano-Sheets with Enhanced Thermoelectric Properties

Songbai Hu, Wenqiao Han, Xiaowen Li, Yanjiang Ji, Mao Ye, Cai Jin, Qi Liu, Sixia Hu, Junling Wang, Jiaqing He, Yuanmin Zhu, Claudio Cazorla, Lang Chen*

Dr. S. Hu, Mr. W. Han, Dr. X. Li, Mr. Y. Ji., Dr. M. Ye, Mr. C. Jin, Dr. Q. Liu, Prof. J. Wang, Prof. J. He, Prof. L. Chen
Department of Physics, Southern University of Science and Technology, Shenzhen 518055, China.
E-mail: chenlang@sustech.edu.cn

Dr. Y. Zhu
School of Material Science and Engineering, Dongguan University of Technology, Dongguan, 523000, China

Ms. S. Hu
Core Research Facilities, Southern University of Science and Technology, Shenzhen 518055, China.

Dr. C. Cazorla
Departament de Física, Universitat Politècnica de Catalunya, Campus Nord B4-B5, E-08034 Barcelona, Spain

Keywords

Abstract

Oxygen vacancy ($V_O^{\bullet\bullet}$) plays a key role in controlling the structures and properties of thermoelectric oxides. However, in misfit-layered compounds vast control of oxygen deficiency remains a big challenge and its effects on the thermoelectric performances has yet to be understood. In this work, we have synthesized $Sr_2O_2H_2]_{0.5}CoO_2$, $[Sr_2O_2]_{0.405}CoO_2$ and $[Sr_2CoO_3]_{0.569}CoO_2$ thin films from insulating brownmillerite $SrCoO_{2.5}$. By modifying the integrated rock salt nano-blocks, the one with the zero-charged $[Sr_2O_2]$ sheets greatly promoted the oxygen deficiency to 2.95 and thus demonstrated the best *PF* (3.6 mWK^{-2}m^{-1}) and κ (0.33 WK^{-1}m^{-1}) at room temperature comparing to the rest. The trimmed physical and chemical properties by different composite laminates and oxygen deficiency remark an efficient strategy in enhancing the room temperature performances in thermoelectric oxides beyond doping or strain engineering.

Main text

Oxygen vacancy ($V_O^{\bullet\bullet}$) plays a key role in controlling the structures and properties of $3d$ transition-metal oxides.[1-12] It has been intensively studied in oxygen deficiency (δ) tuned ferromagnetism,[13-15] insulator-to-metal transition,[16-18] electrochemical catalysis[19-21] and fuel cells[22, 23]. In thermoelectric oxides, oxygen deficiency becomes essentially important as it unavoidably affects the structure and composition stability during the manufacturing or working on the one hand; on the other hand, it controls the valence state of metal ions which directly determine the electric conductivity (σ) and the Seebeck coefficient (S) that is inversely related to the former.[24-30] Generally speaking, higher δ leads to lower σ in $3d$ transition-metal oxides [1, 18, 24, 30-34] and a consequent higher S. In addition, it was found that point defects alone, like oxygen vacancies, typically act as efficient phonon scattering centers, which reduce the phonon mean-free paths and thus deplete the corresponding lattice thermal conductivity (κ)[25, 35]. Therefore, to achieve an excellent figure of merit ZT ($=S^2T\sigma\kappa$, where T is the absolute temperature), the δ should be as high as possible if it does not harm the σ.

In the last decades, dozens of thermoelectric oxides like n-type perovskite $CaMnO_{3-\delta}$,[26, 36, 37] $SrTiO_{3-\delta}$,[27-29, 38] $Cd_3TeO_{6-\delta}$,[39] p-type misfit-layered (ML) $NaCo_2O_{4+\delta}$,[40-42] $Ca_3Co_4O_{9+\delta}$,[43-45] $Bi_2Sr_2Co_2O_{8+\delta}$,[34] $SrCoO_{3-\delta}$,[46, 47] has been synthesized. However, the off-stoichiometry was limited in very small range (<0.5) even under extreme synthesis environments, especially for the p-type ML compound.[33, 34, 46, 47] ML structure is composed by a conductive CdI_2-type CoO_2 layer and an insulating rock salt (RS) layer whom share common a, c axes, but differ in length of b-axis, thus misfit in that direction. This structure demonstrates great advantages in achieving remarkable thermoelectric performances by allowing the improvement of power factor (PF, $=S^2\sigma$) in the CoO_2 layer while suppressing the thermal conductivity at the CoO_2/RS interface.[38, 48, 49] Unlike the oxygen content in perovskite which is solely determined by the valence state of transition-metal ions, in ML structure it also depends on the composite and dimension of integrated RS nano-sheets.[50] For a ML $[A_xB_yO_z]_qCoO_2$, where A and B represents different cations and q [$=b_{CoO2}/b_{RS}$] is the misfit number, the oxygen deficiency will be maximized when the valence of RS-$[A_xB_yO_z]_q$ can be minimized, that is, zero or even negative valence for $[A_xB_yO_z]$. Unfortunately, to date nearly all reported ML compounds sandwich positively

charged RS plate. Thus, the vast control of oxygen deficiency remains a big challenge in and its effects on the thermoelectric performances has yet to be explored.

In this work, we reported a vast control of oxygen deficiency in three systematically synthesized misfit-layered Sr-Co-O thin films (ML-SCO). By modifying the integrated RS nano-blocks, we have obtained ML-SCO with the zero-charged rock salt nano-blocks thus greatly promoted the δ to 2.95. In consequence, the thermoelectric performances were significantly enhanced comparing to the rest.
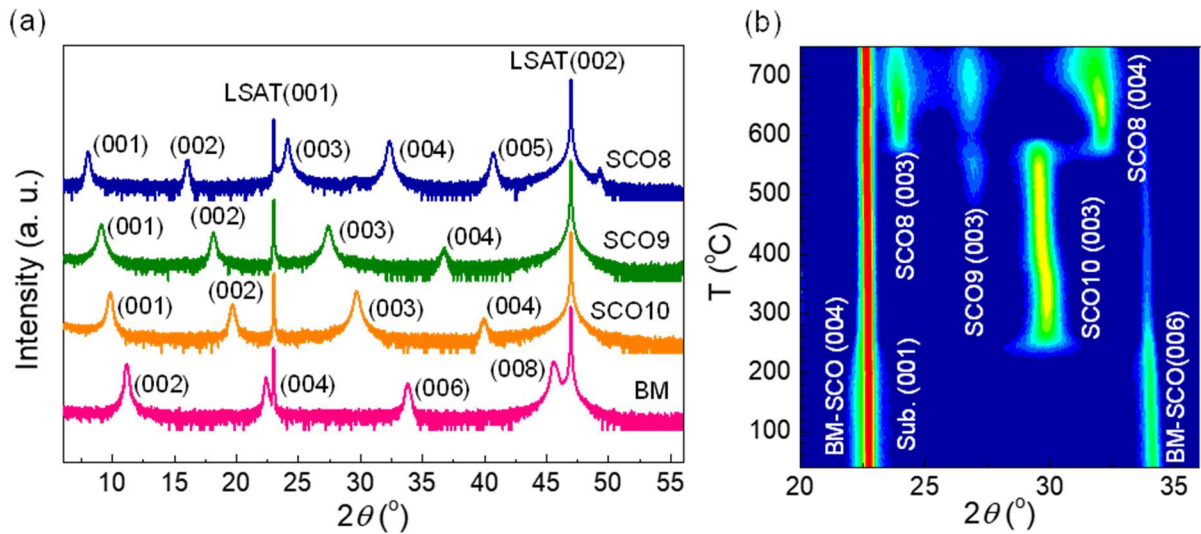

Figure 1. a) XRD θ-2θ scans of as-prepared BM-SCO, SCO10, SCO9 and SCO8 thin films grown on LSAT substrates. b) XRD peak evolution of BM-SCO thin film by heating the sample in wet air.

Bulk BM-SCO is orthorhombic with lattice constants of a = 5.5739 Å, b = 5.4697 Å and c = 15.7450 Å, which can be viewed as pseudo-tetragonal (a_t = 3.905 and c_t = 7.872 Å)[1]. BM-SCO is a reduced form of the perovskite $SrCoO_3$ that is characterized by columns of ordered oxygen vacancy ($V_O^{\bullet\bullet}$) along its pseudo-tetragonal [110] direction [51, 52], which offers an X-ray detectable structure feature for the oxygen evolution. **Figure 1**a) shows the XRD θ-2θ scans of parent BM-SCO thin film and three derived ML-SCO thin films (SCO10, SCO9 and SCO8, named by their lowest diffraction angles which are approximate 10°, 9° and 8°, respectively) grown on (La,Sr)(Al,Ta)O_3 (LSAT) substrate. The trend that 2θ shifts to the lower angle indicates a decreasing and tunable periodicity in Sr-Co-O thin films by temperature control. Correspondingly, the c-lattice constant increases from 9.04 Å to 9.77 Å, and then to 11.06 Å

step by step. Figure 1b) illustrates the XRD peak evolution of BM-SCO thin film by heating the sample in wet air (relative humidity ≈ 79%). At 250 °C the BM-SCO transformed to SCO10. As depicted elsewhere, BM-SCO took in H_2O and transformed to SCO10 when annealed in 1 bar O_2+H_2O.[53] Here due to the relative low humidity of air, a small portion of BM-SCO bottom layer was still observable after 250 °C. At 480 °C, SCO10 started to transformed to SCO9. Meanwhile, the H^+ completely released from the thin film in the form of H_2O, thereafter no protons exist in SCO9 and SCO8. By further annealing the thin film at 580 °C, the SCO10 disappeared and SCO8 began to form. Although mixed phases were observed during the fast linear heating process, pure phases could be obtained by annealing the sample for a longer time (see Experimental section). The temperature dependent XRD confirmed the successive synthesis of the ML-SCO phases from the parent BM-SCO in humid air, in stark contrast with that BM-SCO transform to hexagonal $Sr_6Co_5O_{15}$ when heating in dry air.[54]

The in-plane crystallographic geometry of SCO10, SCO9 and SCO8 are determined by the wide area reciprocal space mapping (WARSM) in **Figure. S1**. It is found that two different crystallographic geometries, i.e., triclinic (T) and hexagonal (H) layers and their 90° rotation counterpart, coexist in each phase pure thin film, which corresponds to the RS layer and the CdI$_2$-type CoO$_2$ layer, respectively. The four-fold geometry of RS layered and six-fold geometry of CoO$_2$ layer are confirmed by the in-plane phi-scans in **Figure S2**. These two geometries can be orthogonalized in in-plane directions by their diagonals, and the lattice parameters a (= $d_{RS(110)} = d_{CoO2(01\bar{1}0)}$) and b (=d_{RS}) = $2d_{CoO\ (21\bar{3}0)}$) are directly calculated from the in-plane θ-2θ scans in **Figure S3**. The epitaxial relationship between the ML-SCO thin films and the LSAT substrate are RS [110] ‖ CoO$_2$ [01$\bar{1}$0] ‖ LSAT [110] and RS [1$\bar{1}$0] ‖ CoO$_2$ [21$\bar{3}$0] ‖ LSAT [1$\bar{1}$0], see **Figure S4**. The lattice parameters are summarized in **Table 1**. In out-of-plane direction, the c of these ML-SCO thin films increases linearly upon annealing at different temperature. In in-plane directions, the a and b of CoO$_2$ layer change slightly for SCO10, SCO9 and SCO8, implying that the hexagonal lattice frame of the ML-SCO thin film is quite stable upon thermal annealing. However, that of the RS layers greatly vary between the three, thus provides tunable axis by modifying the integrated RS nano-blocks.
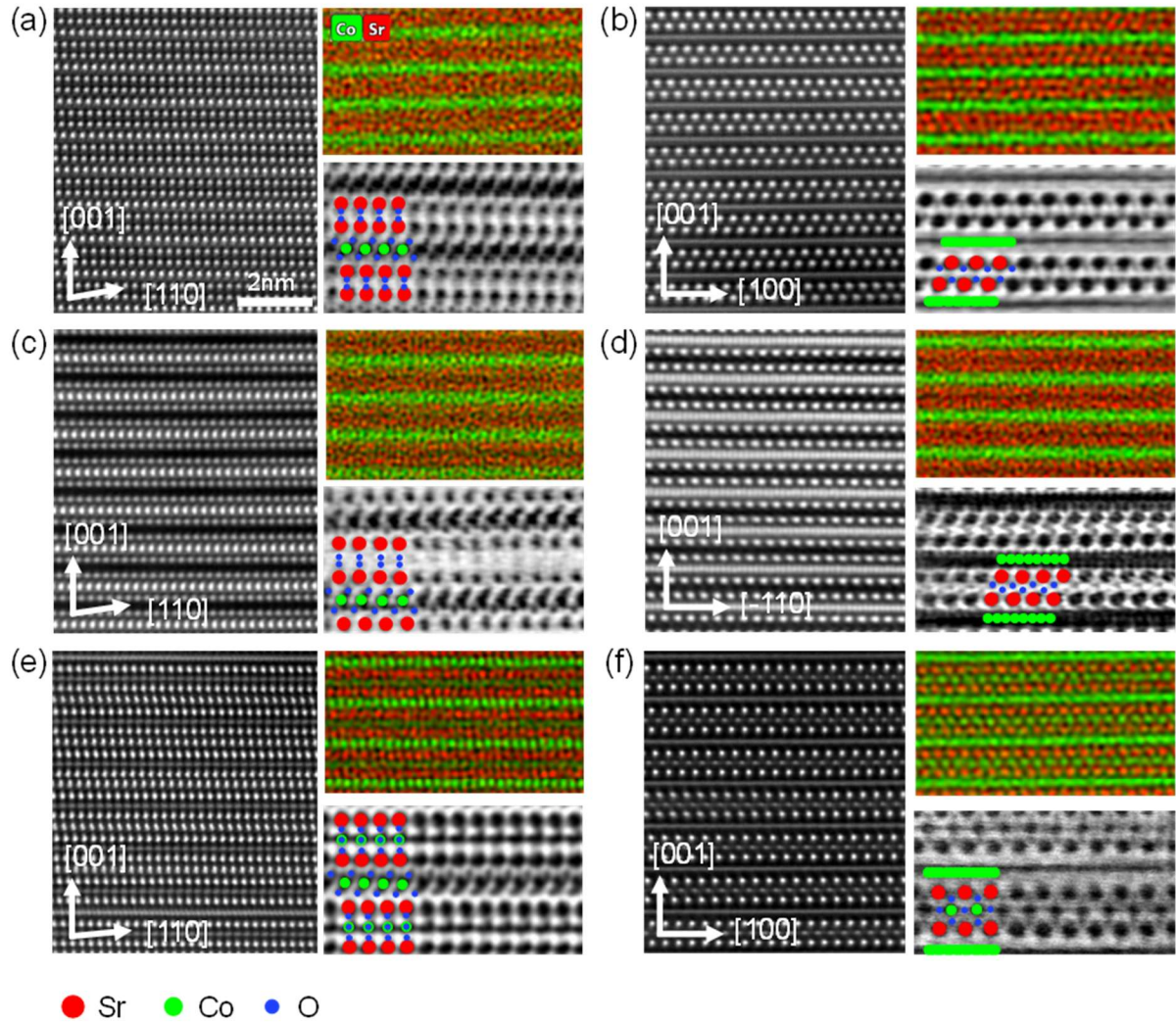
Figure 2. HADDF-STEM, EDS mapping and ABF images for ML-SCO thin films: a) (110) and b) (100) plane of SCO10; c) (110) and d) ($\bar{1}$10) plane of SCO9; e) (110) and f) (100) plane of SCO8. The Sr, Co and O atoms are painted by red, green and blue, respectively.

High resolution STEM (HR-STEM) was carried out to determine the atomic structure of these ML-SCO thin films. **Figure 2** displays the High-Angle Annular Dark Field (HADDF)-STEM, Energy Disperse X-ray Spectroscopy (EDS) mapping and Annular Bright Field (ABF) images for SCO10, SCO9 and SCO8. Figure 2a) & b) show the (110) and (100) atomic planes of SCO10, respectively. The SCO10 thin film has been identified as layered $SrCoO_3H$ with alternatively stacking of rock-salt type triclinic $Sr_2O_2H_2$ and CdI_2-type hexagonal CoO_2 layers elsewhere.[53] Figure 2c) & d) show the (110) and ($\bar{1}$10) atomic planes of SCO9, respectively. The SCO9 was obtained by dehydrating SCO10 at 550 °C. We imaged the ($\bar{1}$10) rather than the (100) plane by considering that the (100) plane rotates too much (~10º, see Figure S1) from the

LSAT (100). Compared to SCO10, a dark strip within the Sr_2O_2 layer is observed after the H_2O dissolution in the HADDF image. The ABF image shows that oxygen atoms in Sr_2O_2 layer of SCO9 take much more spacing along [001] direction than that in SCO10 between the neighboring Sr layers, which is responsible for the increase in c-lattice constant. Meanwhile, the Sr-Sr distance along the b-axis increases dramatically from 2.804 Å in SCO10 to 3.47 Å in SCO9. Such a lattice expansion indicates that there may be a considerable number of $V_O^{\bullet\bullet}$ in SCO9. Figure 2e) & f) show the (110) and (100) atomic plane of SCO8, respectively. Compared to SCO10 and SCO9, an additional Co-O layer is captured within the Sr_2O_2 layer. The corresponding EDS mapping shows that the Co atom occupies the body center of Sr cube. The ABF images show that the oxygen arrangement in SCO8 follows the rock-salt stacking manner as well. Thus, this layer is identified to be Sr_2CoO_3, while the CoO_2 layer remains unchanged. The γ angle between a and c in these ML-SCOs is determined by the fast flourier transformation (FFT) of the (110) atomic plane in **Figure S5**. The atomic structure of the three ML-SCOs are built up based on the XRD and HR-STEM, and are shown in **Figure 5**b) ~ d).

The general formula of these ML-SCO thin films can be described by a $[M_{m+n}Sr_2O_{m+2}]_qCoO_2$, where M represents H or Co, and q [$= 0.5b_{CoO2}/b_{RS}$] is the misfit number. For SCO10, M=H, m=0, n=2, q=0.5; for SCO9, m=0, n=0, q=0.405; for SCO8, M=Co, m=1, n=0, q=0.569. Thus, their formulas can be written as $[Sr_2O_2H_2]_{0.5}CoO_2$ ($SrCoO_3H$), $[Sr_2O_2]_{0.4}CoO_2$ ($Sr_4Co_5O_{14}$) and $[Sr_2CoO_3]_{0.57}CoO_2$ ($Sr_3Co_4O_{9.75}$), assuming that there is free of $V_O^{\bullet\bullet}$ in each sub-layer. The averaged valence state of Co ions [V(Co)] for each of the ML-SCO thin film is thereby determined to be +3, +4 and +3.375, respectively. However, from the preparation point of view, the oxidization from Co^{3+} to Co^{4+} ions by only air-annealing were an arduous work[1, 55]. Thus, the formation of Co^{4+} in SCO9 was less-likely. Here we properly exclude the formation of Sr vacancies by considering that Sr is nonvolatile and that the successive preparation of from $SrCoO_{2.5}$ to $SrCoO_3H$, $Sr_4Co_5O_{14}$ and then $Sr_3Co_4O_{9.75}$ guarantees adequate supply of precursor to the next phase. We would also like to highlight the specialty of structure $[Sr_2O_2]_{0.4}CoO_2$ as its RS layer is electrically zero charged. To date, nearly all reported misfit-layered compounds integrate positively charged RS plate. The SCO9 may produce high concentrate of $V_O^{\bullet\bullet}$ as the nominal 4+ of Co ions is far from the normal 3+ valence state.
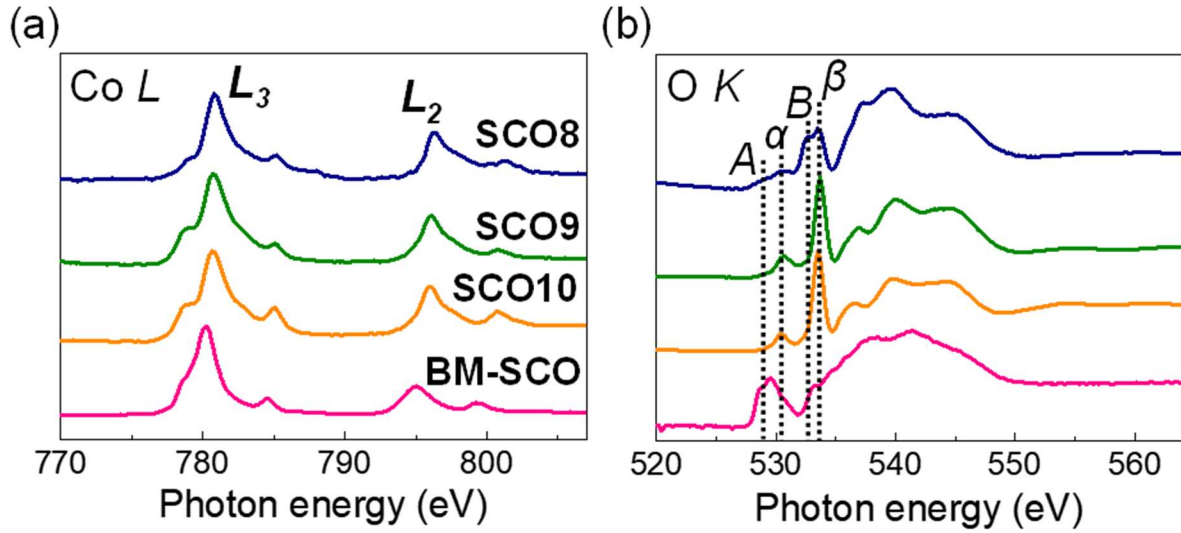
Figure 3. X-ray absorption spectroscopy (XAS) of a) Co L-edge, b) O K-edge for BM-SCO, SCO10, SCO9 and SCO8 thin films.

X-ray absorption spectroscopy (XAS) at the Co L-edge and O K-edge were collected to probed the oxygen deficiency as well as the electronic structures of these SCO thin films. The results in shown in **Figure 3**a) and b), respectively. The XAS of BM-SCO is given for comparison. The schematic electronic structures for [Co(III) $3d$-O $2p$]$_O$, [Co(II) $3d$-O $2p$]$_T$ and [Co(III) $3d$-O $2p$]$_T$ hybridization are shown in **Figure S6**a) ~ c), respectively. The subscript O or T denote the octahedra or triangular crystal ligand field. In the octahedra crystal ligand filed (BM-SCO), the [Co(III) $3d$-O $2p$]$_O$ splits into a high energy e_g band and a low energy t_{2g} band.[56] The transition of the electrons from O $1s$ to the unoccupied t_{2g} and e_g band are represented by A and B, respectively. While in the triangular crystal ligand field (ML-SCO), the t_{2g} band splits into a_{1g} and e_g' bands in further.[57] The transition of electrons from O $1s$ to the unoccupied a_{1g} and t_{2g} band are represented by α, β, respectively. In Figure 3a), the line shapes of Co L-edge in SCO10, SCO9 and SCO8 are quite similar to the Co$_3$O$_4$[58], indicating that there coexist Co(III) and Co(II) in the ML-SCOs. The less pronounced pre-shoulder in Co L-edge of SCO8 is due to that a part of Co ions occupy the octahedral sites in RS Sr$_2$CoO$_3$ layer, thus decreases the number of Co ions in trigonal coordination; while in SCO10 and SCO9 Co ions coordinates only in trigonal coordination.

Figure 3b) shows the evolution of O K-edge of these SCO thin films. In BM-SCO, the electronic configuration in [Co(III) $3d$-O $2p$]$_O$ hybridized orbital is depicted by a high spin

$e_g^2 t_{2g}^4$ (S=5/2) in Figure 3 c).[56] In case of the SCO10, the small bump at low energy side represents the electron transition from the O *1s* to the unoccupied a_{1g} of [Co(II) *3d*-O *2p*]$_T$ hybridized orbital in triangular crystal ligand field.[53] Its week intensity implies that the proportion of Co(II) in SCO10 is fairly small. The strong peak β mixes the contribution from the transition to the e_g of [Co(II) *3d*-O *2p*]$_T$ and [Co(III) *3d*-O *2p*]$_T$. Therefore, the electronic configuration of SCO10 is primarily a null spin state $e_g^0 a_{1g}^2 e_g'^4$ mixed with a small portion of low spin state $e_g^2 a_{1g}^1 e_g'^4$. It is worthy to mention that sole intermediate spin of Co^{3+} ($e_g^1 a_{1g}^1 e_g'^4$) alone can also generate similar feature $\alpha+\beta$. However, further experiment by annealing SCO10 in 10 bar oxygen showed that the feature α presented in vacuum annealed sample disappeared when the Co^{2+} was oxidized to Co^{3+} (**Figure S7**). That means the bump at the low energy side of O K-edge arises only from Co^{2+}. In that sense, the amount of Co(II) can be roughly estimated to 16% using the intensity ratio $\alpha/(\alpha+\beta)$. The averaged valence state of Co ions in CoO$_2$ layer [V(Co)] is thus determined as +2.84. The chemical composition of SCO10 is thereby SrCoO$_{2.92}$H. Similarly, in SCO9 the content of Co(II) is estimated to be approximate 18%, and V(Co) = +2.82. The formular of SCO9 is thereby written as Sr$_4$Co$_5$O$_{11.05}$ accordingly. In SCO8, additional features A and B which has the same peak positions as the BM-SCO were observed as the RS Sr$_2$CoO$_3$ layer was sandwiched in between CoO$_2$ triangular layers except for features α and β. In CoO$_2$ layer the concentration of Co(II) is estimated to be 11%, and the V(Co) = +2.93, assuming that the Co ions in Sr$_2$CoO$_3$ layer are +3 in approximate. The SCO8 is actually Sr$_3$Co$_4$O$_{8.86}$. According to XAS, the oxygen off-stoichiometry in the CoO$_2$ hexagonal layer greatly varies between these ML-SCO thin films, from 0.08 (SCO10) to 2.95 (SCO9) and then to 0.89 (SCO8). Table 1 summarizes the lattice parameters, composition, *V(Co)* and oxygen deficiency (δ) for the three ML-SCO thin films.

Table 1. Structure and composition parameters of ML-SCO thin films

	layer	a (Å)	b (Å)	c (Å)	α/γ (°)	β (°)	q	Formula	$V(Co)$ nominal	$V(Co)$ actual	δ
SCO10	Sr$_2$O$_2$H$_2$	2.518	2.804	9.08	90	95.5	0.500	SrCoO$_{3-\delta}$H	+3	+2.84	0.08
	CoO$_2$	2.518	2.802								
SCO9	Sr$_2$O$_2$	2.449	3.470	9.76	90	96	0.405	Sr$_4$Co$_5$O$_{14-\delta}$	+4	+2.82	2.95
	CoO$_2$	2.449	2.816								
SCO8	Sr$_2$CoO$_3$	2.469	2.469	11.06	90	94.3	0.569	Sr$_3$Co$_4$O$_{9.75-\delta}$	+3.375	+2.93	0.89

CoO$_2$ 2.469   2.808
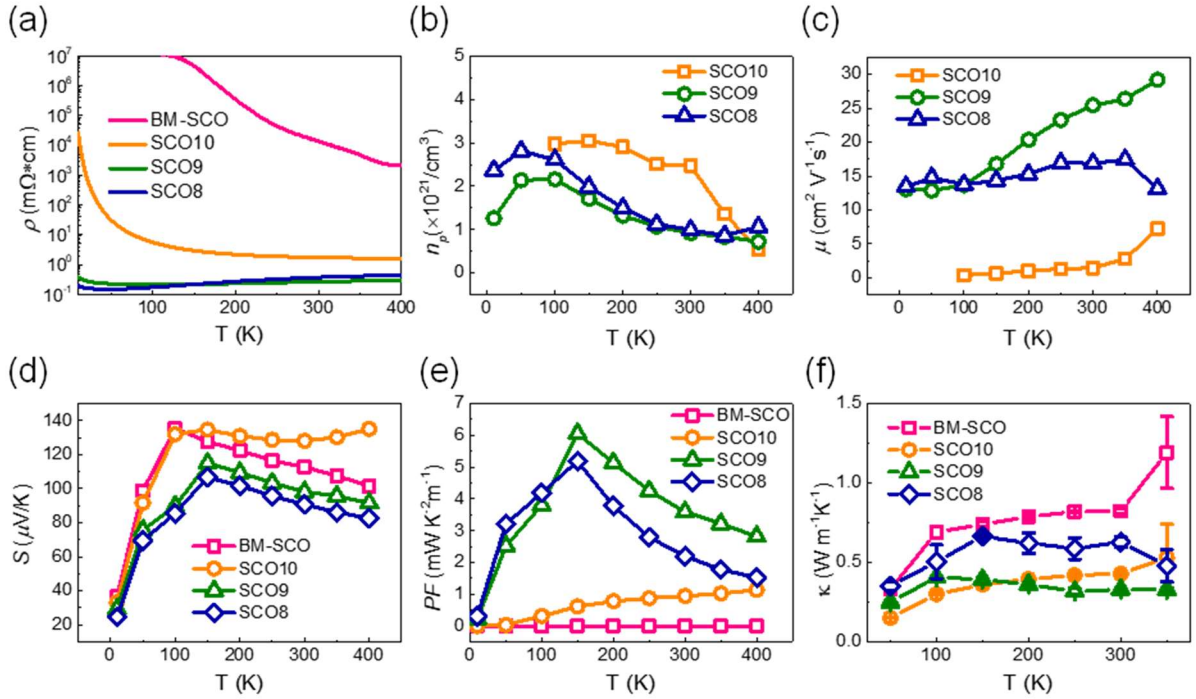
Figure 4. Temperature dependent a) ρ, b) n_p, c) μ, d) S, e) PF and f) κ of BM-SCO and ML-SCO thin films. The error bar in d) represents the standard deviation of three different measurements.

Figure 4 presents the temperature dependent resistivity (ρ, $=1/\sigma$), carrier concentration (n_p) and mobility (μ), S, PF and κ of the BM-SCO and ML-SCO thin films. Figure 4a) demonstrates a clear insulator-to-metal transition when the BM-SCO transformed to SCO10 and then to SCO9/SCO8. That means the electric conductivity of the SCO9 and SCO8 was not harmed even high concentration of $V_O^{\bullet\bullet}$ presents in the thin films. Figure 4b) shows that the n_p in of all three ML-SCO thin films are at the level of 10^{21}/cm^3, which is similar to the NaCo$_2$O$_4$ and Ca$_3$Co$_4$O$_9$. Using $\mu = (\rho n_p e)^{-1}$, where e is the electron charge, the carrier mobility was calculated in Figure 4c). It is found that the μ of SCO9 > SCO8 > SCO10 above 150 K. Therefore, the increase in conductivity is mainly attributed to the increase in carrier mobility rather than carrier concentration, which is generally desired in thermoelectric materials, since an increase in carrier concentration tends to lead to a decrease in the Seebeck coefficient. Figure 4d) shows the experimental S of BM-SCO and ML-SCOs over the temperature interval 400 ~ 10 K. The S positive sign implies that both BM-SCO and ML-SCO thin films are p-type conductors.

Although the conductivity of SCO10 improves 3 orders of magnitude compared to the BM-SCO, its S exhibits even larger value than that of BM-SCO. As a result, the negligible PF in BM-SCO is greatly enhanced to 0.9 mWK^{-2}m^{-1} in SCO10 at 300 K (Figure 4e)). By further modifying the integrated nano-blocks, the S of SCO9 and SCO8 exhibit only a slight suppression, but the conductivity improves another 1 orders of magnitude. Consequently, the PF of SCO9 and SCO8 amount to 3.6 mWK^{-2}m^{-1} and 2.1 mWK^{-2}m^{-1} at 300 K, respectively. Such performances are superior than that of $(Ca_{0.9}M_{0.1})MnO_3$[6], $Ca_3Co_4O_9$[44], ZnO[59] and at the same level to the $NaCo_2O_4$. Figure 4f) shows that the κ of the four SCOs order in SCO9<SCO10<SCO8<BM-SCO above 150 K. Owing to the unique alternative stacking of the insulative and conductive layers, all ML-SCO thin films display significantly decreased thermal conductivity. At room temperature the κ of the four SCO9 lowers down to 0.33 WK^{-1}m^{-1}. By modifying the integrated nano-blocks, the thermoelectric performances of these ML-SCOs were greatly enhanced compared to the BM-SCO through the improvement of electric conductivity and suppress of thermal conductivity. Among them, the SCO9 demonstrate the best PF and κ, followed by the SCO8 and then SCO10.
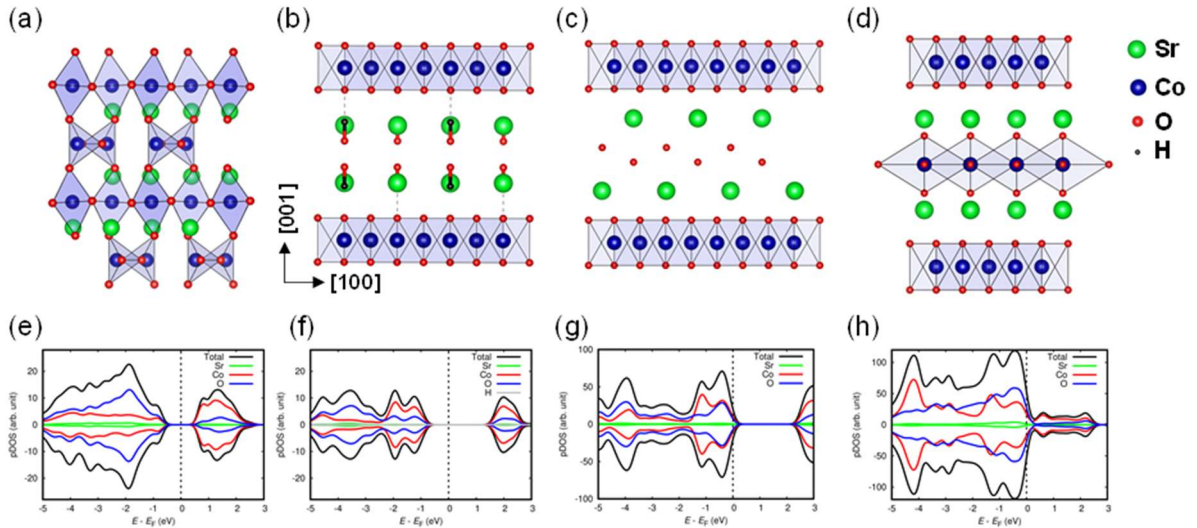

Figure 5. Atomic structures of a) BM-SCO (110), b) SCO10 (100), c) SCO9 (100) and d) SCO8 (100) plane. The corresponding pDOS are given in e), f), g) and h), respectively.

In order to understand the how the rock-salt nano-sheets modify the electric and thermoelectric properties, we carried out DFT based first principle calculations for stoichiometric SCOs. Figure 5 shows the (100) atomic plane of BM-SCO, SCO10, SCO9 and

SCO8 as well as their projected density of states (pDOS) correspondingly. The (010) atomic plane is shown in **Figure S8**. The pDOS shown in Figure 5e), f), g) and h) exhibit a clear trend that the fermi level shifts toward the valence band from BM-SCO, SCO10 to SCO9 and SCO8, indicating a change from insulator to strong p-type conduction, which favors the insulator-to-metal transition that observed in Figure 3a). The SCO8 even switches to metallic as the band gap was closed, which probably attributes to the introduce of Co ions into the Sr_2CoO_3 RS layer. Anyhow, this change does not suppress its S significantly as they arise from different layers. The import of oxygen vacancies into the material can be viewed as doping of hole acceptors which tend to reduce the valence of metal ions. Consequently, the fermi level moves away from the valence band thus results in suppress of electric conduction. However, experimentally we still observed favorable electric conduction even in high $V_O^{\bullet\bullet}$ concentration doped SCO9 and SCO8, which was probably benefit from the intrinsic strong p-type conduction of SCO9 and metallic conduction of SCO8, respectively.

We also calculated the elastic constants and sound velocities for the three ML-SCO polymorphs, see **Table S1**. It shows that SCO9 presents the smallest the sound velocities and Debye temperature. Together with the large amount of oxygen vacancies presented in the thin film which efficiently scatter the phonons, SCO9 exhibits the lowest κ of all three polymorphs, followed by SCO8 and SCO10.

In summary, three ML-SCO polymorphs (SCO10, SCO9 and SCO8) with consecutively increasing out-of-plane d-spacing are synthesized from the brownmillerite $SrCoO_{2.5}$ thin films. These phases consisted of alternatively stacking of RS nano-blocks and CoO_2 frame layer, i.e., $[Sr_2O_2H_2]_{0.5}CoO_2$, $[Sr_2O_2]_{0.405}CoO_2$ and $[Sr_2CoO_3]_{0.569}CoO_2$. XAS reveals that there is a large number of $V_O^{\bullet\bullet}$ ($\delta = 2.95$) in SCO9 as the integrated RS nano-block ($[Sr_2O_2]$) is zero charged. Compared to the BM-SCO parent phase, the thermoelectric performances of all ML-SCO thin films are significantly enhanced, and the films with the most δ (2.95) exhibited the best PF (3.6 $mWK^{-2}m^{-1}$) and κ (0.33 $WK^{-1}m^{-1}$) at room temperature comparing to the rest. Owing to the intrinsic strong p-type conduction, the oxygen deficiency which suppresses the κ in SCO9 and SCO8 does not harm the electric conductivity, but remain metallic even with high concentration. The trimmed physical and chemical properties by different composite laminates and oxygen deficiency remark an efficient strategy in enhancing the thermoelectric performances in oxides

beyond doping or strain engineering.

Experimental Section

The BM-SCO thin films were deposited on LSAT by pulsed laser deposition (PLD). The growth conditions were a temperature of 750°C, oxygen pressure of 13 Pa, laser energy density of 1.5 J/cm^2, and laser frequency of 6 Hz. The film thickness is approximately 70 nm for 4000 pulses deposition. The SCO10 was obtained by annealing BM-SCO in 10 bar CO_2+H_2O at 450 °C for 1 hour, and then in air at 400 °C for another hour. The SCO10 transformed to SCO9 by annealing the sample in air at 550 °C. The SCO8 was obtained by further annealing the SCO9 thin film in air at 700 °C. The sample structure was characterized by a high-resolution X-ray diffractometer (Rigaku SmartLab). HAADF-STEM and EDS were conducted using a double aberration-corrected transmission electron microscopy (Thermo Fisher Themis Z G2 60-300) operated at 300 kV. The XAS was taken at beamline 4B9B of Beijing Synchrotron Radiation Facility in the total fluorescence yield mode (TFY). The Seebeck coefficient, resistivity and Hall measurement of the thin films were measured using a Quantum Design PPMS in a four probes method. The resistance of BM-SCO was measured by a Keithley 6517B picometer with a two-probe connection. The room temperature Seebeck coefficient was verified using a portable thermoelectric monitor (PTM-3, JouleYacht, China). The thermal conductivity was measured by a time-dependent thermal reflectivity (TDTR) method mentioned in elsewhere.[60]

First-principles calculations: Spin-polarised density functional theory (DFT)[61] calculations were performed to theoretically characterise the structural, mechanical and electronic properties of SCO polymorphs. We used the PBEsol functional[62] as implemented in the VASP software[63] . A "Hubbard-U" scheme[64] with $U = 4$ eV was employed for a better treatment of the localized Co $3d$ electronic orbitals[65]. We used the "projector augmented wave" method to represent the ionic cores[66] by considering the following electrons as valence: Sr $4s$, $4p$, and $5s$; Co $3d$ and $4s$; O $2s$ and $2p$; H $1s$. Wave functions were represented in a plane-wave basis truncated at 650 eV. For integrations within the first Brillouin zone we employed thick Monkhorst-Pack k-point grids with a density equivalent to that of 16x16x16 for a conventional 5-atoms perovskite unit cell. Periodic boundary conditions were applied along the three lattice vectors of the simulation supercell. Geometry relaxations were performed with a conjugate-

gradient algorithm that optimized the ionic positions and the volume and shape of the simulation cell. The relaxations were halted when the forces in the atoms were all below 0.005 eV·Å^{-1}. By using these technical parameters, the obtained energies were converged to within 0.5 meV per formula unit. Different possible spin magnetic arrangements involving the electronic Co d orbitals (i.e., ferromagnetic and antiferromagnetic type A, C and G[67]) were explored in our DFT calculations. For the calculation of electronic densities of states, we employed the more accurate range-separated hybrid functional HSE06[68].

References

[1] H. Jeen, W. S. Choi, J. W. Freeland, H. Ohta, C. U. Jung, H. N. Lee, *Adv. Mater.* **2013**, 25, 3651.

[2] L. Cao, O. Petracic, P. Zakalek, A. Weber, U. Rücker, J. Schubert, A. Koutsioubas, S. Mattauch, T. Brückel, *Adv. Mater.* **2019**, 31, 1806183.

[3] A. Khare, D. Shin, T. S. Yoo, M. Kim, T. D. Kang, J. Lee, S. Roh, I.-H. Jung, J. Hwang, S. W. Kim, T. W. Noh, H. Ohta, W. S. Choi, *Adv. Mater.* **2017**, 29, 1606566.

[4] D. Li, K. Lee, B. Y. Wang, M. Osada, S. Crossley, H. R. Lee, Y. Cui, Y. Hikita, H. Y. Hwang, *Nature* **2019**, 572, 624.

[5] D. A. Muller, N. Nakagawa, A. Ohtomo, J. L. Grazul, H. Y. Hwang, *Nature* **2004**, 430, 657.

[6] L. Malavasi, C. A. J. Fisher, M. S. Islam, *Chem. Soc. Rev.* **2010**, 39, 4370.

[7] D. Poetzsch, R. Merkle, J. Maier, *Adv. Funct. Mater.* **2015**, 25, 1542.

[8] S. Hu, J. Seidel, *Nanotechnology* **2016**, 27, 325301.

[9] Q. Lu, B. Yildiz, *Nano. Lett.* **2016**, 16, 1186.

[10] N. Zhang, Y. Zhu, D. Li, D. Pan, Y. Tang, M. Han, J. Ma, B. Wu, Z. Zhang, X. Ma, *ACS Appl. Mater. Interfaces* **2018**, 10, 38230.

[11] J. Song, Y. Chen, H. Zhang, F. Han, J. Zhang, X. Chen, H. Huang, J. Zhang, H. Zhang, X. Yan, T. Khan, S. Qi, Z. Yang, F. Hu, B. Shen, J. Sun, *Phys. Rev. Mater.* **2019**, 3, 045801.

[12] S. Inkinen, L. Yao, S. van Dijken, *Phys. Rev. Mater.* **2020**, 4, 046002.

[13] C. Bi, Y. Liu, T. Newhouse-Illige, M. Xu, M. Rosales, J. W. Freeland, O. Mryasov, S. Zhang, S. G. E. te Velthuis, W. G. Wang, *Phys. Rev. Lett.* **2014**, 113.

[14] H.-B. Li, N. Lu, Q. Zhang, Y. Wang, D. Feng, T. Chen, S. Yang, Z. Duan, Z. Li, Y. Shi, W. Wang, W.-H. Wang, K. Jin, H. Liu, J. Ma, L. Gu, C. Nan, P. Yu, *Nat. Commun.* **2017**, 8.

[15] D. A. Gilbert, J. Olamit, R. K. Dumas, B. J. Kirby, A. J. Grutter, B. B. Maranville, E. Arenholz, J. A. Borchers, K. Liu, *Nat. Commun.* **2016**, 7.

[16] Y. B. Nian, J. Strozier, N. J. Wu, X. Chen, A. Ignatiev, *Phys. Rev. Lett.* **2007**, 98, 146403 (

[17] J. Jeong, N. Aetukuri, T. Graf, T. D. Schladt, M. G. Samant, S. S. P. Parkin, *Science* **2013**, 339, 1402.

[18] N. Lu, P. Zhang, Q. Zhang, R. Qiao, Q. He, H.-B. Li, Y. Wang, J. Guo, D. Zhang, Z. Duan, Z. Li, M. Wang, S. Yang, M. Yan, E. Arenholz, S. Zhou, W. Yang, L. Gu, C.-W. Nan, J. Wu, Y. Tokura, P. Yu, *Nature* **2017**, 546, 124.

[19] U. Dey, S. Chatterjee, A. Taraphder, *Phys. Chem. Chem. Phys.* **2018**.

[20] A. Grimaud, O. Diaz-Morales, B. Han, W. T. Hong, Y.-L. Lee, L. Giordano, K. A. Stoerzinger, M. T. M. Koper, Y. Shao-Horn, *Nat. Chem.* **2017**, 9, 457.

[21] P. Yan, J. Zheng, Z. K. Tang, A. Devaraj, G. Chen, K. Amine, J. G. Zhang, L. M. Liu, C. Wang, *Nat. Nanotechnol.* **2019**, 14, 602.

[22] Y.-M. Kim, J. He, M. D. Biegalski, H. Ambaye, V. Lauter, H. M. Christen, S. T. Pantelides, S. J. Pennycook, S. V. Kalinin, A. Y. Borisevich, *Nat. Mater.* **2012**, 11, 888.

[23] M. Papac, V. Stevanović, A. Zakutayev, R. O'Hayre, *Nat. Mater.* **2021**, 20, 301.

[24] Q. Lu, S. Huberman, H. Zhang, Q. Song, J. Wang, G. Vardar, A. Hunt, I. Waluyo, G. Chen, B. Yildiz, *Nat. Mater.* **2020**, 19, 655.

[25] G.-K. Ren, J.-L. Lan, K. J. Ventura, X. Tan, Y.-H. Lin, C.-W. Nan, *npj Comput. Mater.* **2016**, 2, 16023.

[26] M. Molinari, D. A. Tompsett, S. C. Parker, F. Azough, R. Freer, *J. Mater. Chem. A* **2014**, 2, 14109.

[27] J. Liu, C. L. Wang, W. B. Su, H. C. Wang, P. Zheng, J. C. Li, J. L. Zhang, L. M. Mei, *Appl. Phys. Lett.* **2009**, 95, 162110.

[28] S. Lee, G. Yang, R. H. T. Wilke, S. Trolier-McKinstry, C. A. Randall, *Phys. Rev. B* **2009**, 79, 134110.

[29] C. Yu, M. L. Scullin, M. Huijben, R. Ramesh, A. Majumdar, *Appl. Phys. Lett.* **2008**, 92, 191911.

[30] Q. Yang, J. Lee, B. Feng, Y. Ikuhara, G. Kim, H. J. Cho, H. Jeen, H. Ohta, *ACS Appl. Electron. Mater.* **2020**, 2, 2250.

[31] M. Shizuya, M. Isobe, E. Takayama-Muromachi, *J. Appl. Phys.* **2007**, 102, 023704.

[32] H.-B. Li, F. Lou, Y. Wang, Y. Zhang, Q. Zhang, D. Wu, Z. Li, M. Wang, T. Huang, Y. Lyu, J. Guo, T. Chen, Y. Wu, E. Arenholz, N. Lu, N. Wang, Q. He, L. Gu, J. Zhu, C.-W. Nan, X. Zhong, H. Xiang, P. Yu, *Adv. Sci.* **2019**, 6, 1901432.

[33] M. Karppinen, H. Fjellvag, T. Konno, Y. Morita, T. Motohashi, H. Yamauchi, *Chem. Mater.* **2004**, 16, 2790.

[34] Y. Morita, J. Poulsen, K. Sakai, T. Motohashi, T. Fujii, I. Terasaki, H. Yamauchi, M. Karppinen, *J. Solid State Chem.* **2004**, 177, 3149.

[35] B. Duan, Y. Li, J. Li, Y. Gao, P. Zhai, J. Yang, Z. Lu, H. Yang, H. Wang, G. Li, *Ceram. Int.* **2020**, 46, 26176.

[36] E. Bakken, T. Norby, S. Stolen, *Solid State Ionics* **2005**, 176, 217.

[37] R. U. Chandrasena, W. Yang, Q. Lei, M. U. Delgado-Jaime, K. D. Wijesekara, M. Golalikhani, B. A. Davidson, E. Arenholz, K. Kobayashi, M. Kobata, F. M. F. de Groot, U. Aschauer, N. A. Spaldin, X. Xi, A. X. Gray, *Nano. Lett.* **2017**, 17, 794.

[38] X.-L. Shi, H. Wu, Q. Liu, W. Zhou, S. Lu, Z. Shao, M. Dargusch, Z.-G. Chen, *Nano Energy* **2020**, 78, 105195.

[39] Y. J. Shan, K. Sasaki, K. Sudo, H. Imoto, M. Itoh, *Jpn. J. Appl. Phys., Part 2* **2002**, 41, L780.

[40] I. Terasaki, Y. Sasago, K. Uchinokura, *Phys. Rev. B* **1997**, 56, 12685.

[41] J. Xin, A. Basit, S. Li, S. Danto, S. C. Tjin, L. Wei, *Sensors* **2021**, 21, 3437.

[42] J. He, Y. Liu, R. Funahashi, *J. Mater. Res.* **2011**, 26, 1762.

[43] S. W. Li, R. Funahashi, I. Matsubara, K. Ueno, H. Yamada, *J. Mater. Chem.* **1999**, 9, 1659.

[44] B. Paul, E. M. Bjork, A. Kumar, J. Lu, P. Eklund, *ACS Appl. Energy Mater.* **2018**, 1, 2261.

[45] X. Zhu, D. Shi, S. Dou, Y. Sun, Q. Li, L. Wang, W. Li, W. Yeoh, R. Zheng, Z. Chen, C. Kong, *Acta Materialia* **2010**, 58, 4281.

[46] H. Yamauchi, K. Sakai, T. Nagai, Y. Matsui, M. Karppinen, *Chem. Mater.* **2006**, 18, 155.

[47] S. Ishiwata, I. Terasaki, Y. Kusano, M. Takano, *Physica C* **2007**, 460, 491.

[48] K. Koumoto, I. Terasaki, R. Funahashi, *MRS Bull.* **2006**, 31, 206.

[49] K. Takahata, Y. Iguchi, D. Tanaka, T. Itoh, I. Terasaki, *Phys. Rev. B* **2000**, 61, 12551.

[50] H. Yamauchi, L. Karvonen, T. Egashira, Y. Tanaka, M. Karppinen, *J. Solid State Chem.* **2011**, 184, 64.

[51] R. K. Y. Takeda, T. Takada, O. Yamamoto, M. Takano and Y. Bando, *Z. anorg. allg. Chem.* **1986**, 9-10, 259.

[52] A. Nemudry, P. Rudolf, R. Schollhorn, *Chem. Mater.* **1996**, 8, 2232.

[53] Y. Z. Songbai Hu, Wenqiao Han, Xiaowen Li, Yanjiang Ji, Mao Ye, Cai Jin, Qi Liu, Sixia Hu, Jiaou Wang, Junling Wang, Jiaqing He, Claudio Cazorla, and Lang Chen, *Adv. Mat.* **2021**, 202104623.

[54] W. T. A. Harrison, S. L. Hegwood, A. J. Jacobson, *J. Chem. Soc., Chem. Commun.* **1995**, 19, 1953.

[55] Y. Long, Y. Kaneko, S. Ishiwata, Y. Taguchi, Y. Tokura, *J. Phys.: Condens. Matter* **2011**, 23, 245601.

[56] S. Hu, W. Han, S. Hu, J. Seidel, J. Wang, R. Wu, J. Wang, J. Zhao, Z. Xu, M. Ye, L. Chen, *Chem. Mater.* **2019**, 31, 6117.

[57] T. Mizokawa, Y. Wakisaka, T. Sudayama, C. Iwai, K. Miyoshi, J. Takeuchi, H. Wadati, D. G. Hawthorn, T. Z. Regier, G. A. Sawatzky, *Phys. Rev. Lett.* **2013**, 111, 056404.

[58] D. K. Bora, X. Cheng, M. Kapilashrami, P. A. Glans, Y. Luo, J. H. Guo, *J. Synchrotron Radiat.* **2015**, 22, 1450.

[59] M. Ohtaki, T. Tsubota, K. Eguchi, H. Arai, *J. Appl. Phys.* **1996**, 79, 1816.

[60] C. Di, J.-H. Pan, S.-T. Dong, Y.-Y. Lv, X.-J. Yan, J. Zhou, S.-H. Yao, H. Lu, V. E. Gusev, Y.-F. Chen, M.-H. Lu, *CrystEngComm* **2019**, 21, 6261.

[61] C. Cazorla, J. Boronat, *Rev. Mod. Phys.* **2017**, 89, 035003.

[62] J. P. Perdew, A. Ruzsinszky, G. I. Csonka, O. A. Vydrov, G. E. Scuseria, L. A. Constantin, X. Zhou, K. Burke, *Phys. Rev. Lett.* **2008**, 100, 136406.

[63] G. Kresse, J. Furthmüller, *Phys. Rev. B* **1996**, 54, 11169.

[64] S. L. Dudarev, G. A. Botton, S. Y. Savrasov, C. J. Humphreys, A. P. Sutton, *Phys. Rev. B* **1998**, 57, 1505.

[65] P. Rivero, C. Cazorla, *Phys. Chem. Chem. Phys.* **2016**, 18, 30686.

[66] P. E. Blochl, *Phys. Rev. B* **1994**, 50, 17953.

[67] C. Cazorla, O. Dieguez, J. Iniguez, *Sci. Adv.* **2017**, 3, e1700288.

[68] J. Heyd, G. E. Scuseria, M. Ernzerhof, *J. Chem. Phys.* **2003**, 118, 8207.

Support Information

Supporting Information is available from the Online Library or from the author.

Conflict of Interest

The authors declare no conflict of interest.